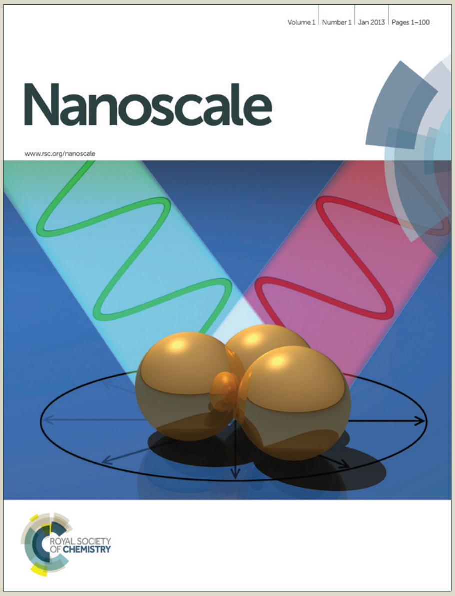

Nanoscale RSCPublishing

ARTICLE

S4Cite this: DOI: 10.1039/x0xx00000x

Received 00th January 2012,
Accepted 00th January 2012

DOI: 10.1039/x0xx00000x

www.rsc.org/

Design and optimization of Lipid-modified poly(amidoamine) dendrimer coated iron oxide nanoparticles as probes for biomedical applications

A. Boni,[a] G. Bardi,[b] A.. Bertero,[c,d] V. Cappello,[a] M. Emdin,[e] A. Flori,[e] M. Gemmi,[a] C. Innocenti,[f] L. Menichetti,[e,g] C. Sangregorio,[h] S. Villa[a] and V. Piazza[a]

Superparamagnetic Iron oxide nanoparticles with a wide size range (2.6-14.1 nm) were synthesized and coated with the amphiphilic Poly(amidoamine) PAMAM-C_{12} dendrimer. The resulting well dispersed and stable water suspensions were fully characterized in order to explore their possible use for biomedical applications. The structural and magnetic properties of the nanoparticles were preserved during the coating and were related to their relaxometric behaviour. The Nuclear magnetic Resonance Dispersion (NMRD) profiles were found to be in accordance with the Roch model. The biocompatibility was assessed by means of cell viability tests and Transmission Electron Microscopy (TEM) analysis. The nanoparticles' capability of being detected *via* Magnetic Resonance Imaging (MRI) was investigated by means of clinical MRI scanners both in water and agar gel phantoms, and in a mouse model.

Introduction

Super Paramagnetic Iron Oxide Nanoparticles (SPIONs) have attracted interest as diagnostic probes for Magnetic Resonance Imaging (MRI).[1] Ultrasmall Super Paramagnetic Iron Oxide Nanoparticles (USPIONs) are able to induce inhomogeneity in the local magnetic field experienced by the surrounding water molecules,[2] thus resulting in shorter T_2 relaxation times of the protons,[3] providing a dark or negative contrast in the T_2-weighted MR images. Synthesizing magnetic nanoparticles possessing appropriate physicochemistry and tailored surface properties allows obtaining of complimentary or alternative MRI probes as compared to other contrast agents such as Gadolinium-Based Contrast Agents (GBCAs).

Precise control over the synthesis conditions and surface functionalization of SPIONs is crucial because it governs their physicochemical properties, their colloidal stability, and their biological behaviour/fate, as well as their magnetic and relaxometric properties. In particular, for MRI purposes, magnetic platforms should possess very small size and narrow size distribution together with high magnetization values. On this purpose, it has to be kept in consideration that size not only affects the relaxivity itself, but it is also a key parameter for the interaction of the nanoparticle with the biological environment, thus determining toxicity and clearance.[4, 5] In order to reach these goals, magnetic nanoparticles are often synthesized by decomposition of organometallic precursors into hot surfactant solutions, a technique that results in highly crystalline iron oxide cores with a narrow and tunable size distribution.[6-9] Additionally, an optimal surface coating is desired in order to preserve the crystalline core, ensure tolerance and biocompatibility, as well as specific localization at the biological target site. Thus, the ideal coating should require a mild attachment process, to preserve the crystalline core, providing a strong bond to the nanoparticles at the same time, to ensure stability in the biological environment. Furthermore, the coating should be chemically versatile and easy to conjugate with diverse molecular moieties for the functionalization of the nanoparticle surface.

In this context, recently some of us reported[10] a novel method to disperse hydrophobic magnetic nanoparticles in water using a modified C_{12}- Poly(amidoamine) (PAMAM) dendrimer as a coating. Dendrimers are highly monodisperse hyperbranched polymers, which display interesting advantages over linear polymers, owning a repetitive and perfectly defined structure in which the number and nature of exposed functional groups can be controlled precisely.[1] Moreover, their ability to promote internalization by endocytosis,[11] makes them a promising tool for therapeutic and diagnostic purposes,[12, 13] with a wide range of potential applications, like intracellular delivery of drugs,[14, 15], genes [16-18] or imaging agents.[19, 20] The reported approach for the coating of NPs with lipid-modified PAMAM dendrimers, which occurs through hydrophobic interaction of the C_{12} chains of the dendrimer with the oleic acid coating, presents important advantages over existing strategies. Firstly, the procedure does not require harsh conditions, thus preserving magnetic and structural properties of the iron oxide nanoparticles, which can be finely tuned by synthesizing the nanoparticles with the decomposition of organometallic precursors. Moreover, the possibility of performing the coating process directly in water/pentane makes it possible to avoid toxic solvents such as DiMethyl SulfOxide (DMSO) and N,N-DiMethyl Formamide (DMF), which are difficult to remove, thus reducing the safety risk deriving from their presence in traces in the final injectable solution. Finally, the mild temperatures required by this method make it possible to use dendrimers modified with thermally unstable moieties, thus extending the range of functional groups that can be conjugated with NPs for targeting or sensing. In summary, this approach provides the possibility to obtain well stable iron oxide nanoparticles water dispersions, conjugated with dendrimers opportunely functionalized with molecules such as fluorophore dyes, drugs or target moieties for specific biomedical applications, such as targeted drug delivery or targeted MRI.

The aim of this work is to use the PAMAM coating as a platform to obtain iron oxide nanoparticles with modulated structural, magnetic and relaxometric properties, and to investigate the possibility to use the obtained materials for biomedical applications. In this paper, we synthesized PAMAM coated iron oxide nanoparticles with a wide range of diameters, in order to optimize the relaxometric performance of this material. The obtained materials have been fully characterized by means of structural (Dynamic Light Scattering, DLS, Transmission Electron Microscopy, TEM), magnetic (SuperConducting Quantum Interference Device, SQUID), and relaxometric (Fast Field Cycling, FFC) techniques. Their biocompatibility has been confirmed by cell viability tests, and their MR contrast efficiency has been evaluated both in phantom solutions and *in vivo*. The large number of parameters here reported and consistently discussed represent the necessary information that should be always provided when new systems based on iron oxide nanoparticles are proposed for a realistic application in the biomedical field.

Results and discussion

Synthesis and structural characterization

Several batches of iron oxide nanoparticles were synthesized according to the method proposed by Hyeon and coworkers.[9] The final products were characterized by TEM analysis. All samples consisted of a dispersion of almost spherical particles, and the size distribution over ca. 200 nanoparticles for each sample could be fit to a Gaussian to obtain the mean diameters, which are reported in Table 1 and Fig. S1 (see Supplementary Material).

By reproducing the experimental conditions reported in the literature, with an iron/surfactant molar ratio of 1:1, 1:2 and 1:3, we obtained samples NP1-3, which displayed a core diameter of 2.6, 5.9 and 8.9 nm, respectively. In order to expand this range, we modified the reaction conditions but found that any decrease of the iron/surfactant molar ratio did not permit to obtain larger nanoparticles. However, with a molar ratio of 1:3, but with a double solvent volume, we obtained a sample of nanoparticles with a mean diameter of 14.1 nm, which was named NP4. In all cases, the size distribution was very narrow, with a standard deviation below 0.9 (see Supplementary Material, Fig. S1). The samples NP1-3 displayed an almost spherical shape, while NP4, due to the larger size, showed preferential growth of certain crystal faces which only slightly altered the shape of the spheres (Fig. 1). Finally, analysis of the electron diffraction patterns demonstrates that the nanoparticles are crystalline and their diffraction pattern is compatible with a cubic magnetite structure for all the considered samples (data not shown).

The coating procedure was performed on the samples NP1-4 by means of the reaction with lipid-modified PAMAM dendrimers of generation 4,[10] which allowed us to obtain stable water dispersions of all the samples, which were named S1-4, respectively. The final water dispersions were characterized by ICP-MS, DLS, and TEM. ICP-MS on the dry powders allowed to confirm the presence of a mono-layer of dendrimers on the nanoparticles' surface, confirming the results reported in a previous paper.[10] DLS analysis was done to measure the average hydrodynamic diameter of PAMAM coated nanoparticles and their stability in time. From the DLS mass distributions, it was observed that the average hydrodynamic diameter was higher than expected by considering the TEM images (see Table 1). However, TEM analysis did not show evidences of aggregates formation, as the particles were uniformly distributed on the grid (see Supplementary Material, Fig. S2). Thus, we should take into account the overestimation provided by the DLS technique, which is affected by problems such as high scattering and double layer surrounding the particles. However further DLS measurements repeated over weeks did not report changes in mean hydrodynamic diameter and allowed to confirm the dispersions stability.

Figure 1. TEM images of samples NP1-4 (all images are taken at the same magnification).

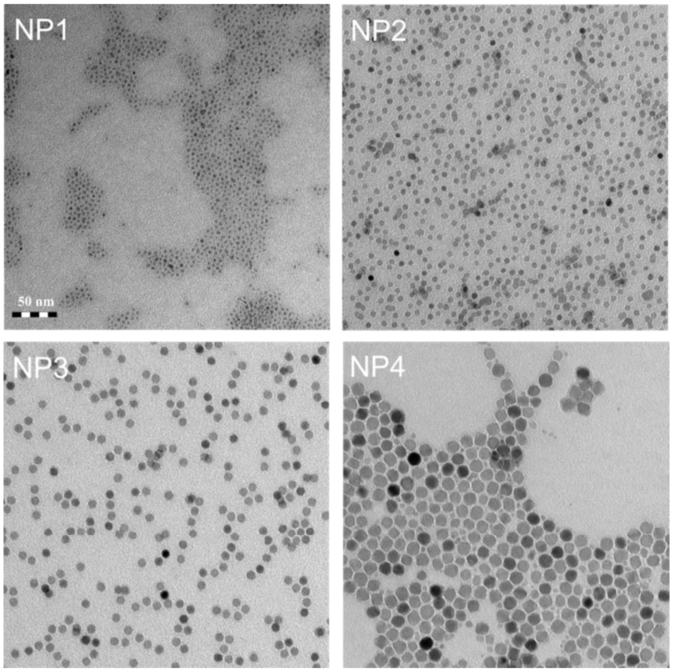

Table 1. Structural paremeters: Core (by TEM) and Hydration mean diameters (by DLS, measured on the respective water suspensions S1-4). Magnetic parameters of the dry powders extracted from ZFC/FC curves and M(H) data: blocking temperature T_b, coercive field H_C, reduced magnetization M_r and saturation magnetization M_S at low and high temperatures. M_S value are reported per gram of magnetic material, Fe_3O_4, as determined by the ICP-MS analysis.

Sample	dcore [nm]	dhyd [nm]	Tb [K]	µ0Hc [Oe]	Mr/Ms	Ms@2.5K [emu g-1]	Ms@300K [emu g-1]
S1	2.6	49.3	5.8	133.2	0.23	49.2	40.0
S2	5.9	84.7	125	417.7	0.25	60.2	51.2
S3	8.9	91.9	147	561.1	0.37	67.3	59.2
S4	14.1	96.1	268	519.9	0.35	75.1	66.7

Furthermore, TEM analysis allowed verifying that the coating step, thanks to the mild reaction conditions, did not alter the structural properties of the samples, and the mean diameters, as well as the electron and X-ray diffraction patterns and the size distributions were unchanged (see Supplementary Material, Fig. S2-3).

In order to investigate the stability of the coating, we decided to introduce gadolinium ions on the PAMAM dendrimer and monitor their concentration in time by means of ICP-MS analysis. The PAMAM dendrimers where reacted with the N-HydroxySuccinimide (NHS) ester derivative of 1,4,7,10-tetraazacycloDOdecane-1,4,7,10-Tetraacetic Acid (DOTA), a well-known complexing agent for lanthanide ions. The modified dendrimers were reacted with an excess of gadolinium trichloride in water, and used to perform the coating of the nanoparticles (sample S3 was chosen) reproducing the conditions described for the unmodified dendrimers. The final product was redispersed in water and recovered with a magnet 4 times, until the Fe/Gd mass ratio reached a stable value of ca. 100. After 3, 30, 45 and 60 days, the nanoparticles were again recovered and redispersed in water to remove eventual lost dendrimers. After 45 days the Fe/Gd ratio was still stable and equal to the initial value, and only after 60 days an alteration of 2% was detected. The high crystallinity of the cores, preserved during the coating process, and the good stability of the coating are key features for *in vivo* applications of the obtained materials.

Magnetic Characterization

In order to confirm the structural evidences and establish the magnetic behaviour of the nanoparticle dispersions, which strongly contribute to their relaxometric performance, a full set of magnetic measurements was performed on the solid (dry powders) of samples S1-4. The main magnetic parameters resulting from these measurements are summarized in Table 1.

The zero-field cooled/field cooled (ZFC/FC) magnetization curves, collected with a probe field of 5 mT in the 2-300K temperature range, are reported in Fig. 2A.

Figure 2. A) ZFC and FC magnetization curves acquired by applying a 5mT probing field, B) M (H) curves measured at 300 K, C) hysteresis cycles at T=2.5K and D) hysteresis cycles detail of the open loops at low magnetic fields, for dry powders of samples S1-4. Data are reported per gram of magnetic material, Fe_3O_4, evaluated from ICP-MS data.

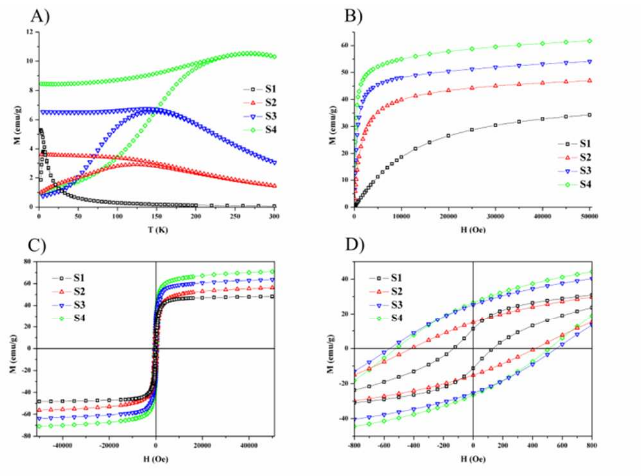

The curves represent the typical behaviour of a set of single domain NPs, whose average blocking temperature, T_b, can be associated to the temperature at which the ZFC curve reaches its maximum. According to the Néel model, T_b is proportional to the anisotropy energy barrier E = KV, where K is the anisotropy constant of the material and V the mean magnetic volume of the NPs. Our results show how T_b increases with size, as expected, reaching the room temperature in the case of sample S4. Furthermore, the irreversibility temperature, where the ZFC and FC curves superimpose, is very close to T_b confirming the narrow size distribution observed in the TEM images. On the other hand, the shape of the FC curve for S4 and, partially for S3, which decreases with decreasing temperature below T_b, suggests that the dipolar interactions are not negligible when these samples, with a large size, are measured as dried powders. The magnetization as a function of the applied field, M(H), was measured at 300 K (Fig. 2B) and 2.5 K (Fig. 2C) up to 5 T. The magnetization curves rapidly approach the saturation, except for sample S1, consistently with a significant surface effect due to the large surface/volume ration of the S1 nanoparticles. However, as the magnetization curves do not completely saturate, an estimate of the saturation value, M_s, was obtained by fitting the high field magnetization data to the empirical law $M = M_s + b/H + c/H^2$. [21] At high temperature, the saturation value varies from 40.0 to 66.7 emu/g of iron oxide upon the particles size increase, as the result of a lower relative amount of a magnetically inactive surface layer, arising from surface crystalline defects (Table 1). Hysteresis was observed at low temperature (Fig. 2D), while no coercivity is present at 300K, as expected for superparamagnetic nanoparticles. This prefigures to use these nanoparticles as negative contrast agents for MRI, as the superparamagnetic behaviour allows a fast response to the applied magnetic field, a large and constant magnetic moment for single particles, and prevents the formation of agglomerates. [22] The coercive field, H_c, and reduced magnetization at low temperature, M_r, = M(0)/M(5T), increase with increasing size along the whole series, apart for S4 for which a slight reduction of both these parameters is observed. The dependency of coercive field and saturation magnetization on the size is consistent with the results reported in the literature.[23,24]

Relaxometry

A relationship between the structural and magnetic properties of the samples and the relaxometric behaviour has been evaluated. The nuclear magnetic relaxation properties of a compound are ideally obtained by the study of its Nuclear Magnetic Resonance Dispersion (NMRD) profile. These curves give the relaxivity evolution versus the external magnetic field, and constitute an interesting tool to optimize the parameters of the nanoparticle synthesis.[25] The relaxivity (r) is defined as the increase of the relaxation rate (R, the inverse of the relaxation time T) of the solvent (water in this case) induced by 1 mM of the active ion (iron in this case).

Fast Field-cycling relaxometry techniques implemented on two different instruments operating in the low field (0.01-20 MHz) and high field (20-70 MHz) ranges were used to acquire longitudinal NMRD r_1 profiles for the S1-4 samples at 1 mM iron concentration over a wide range of magnetic fields (see methods section). The values acquired at 20 MHz with both instruments differ of less than 3%, thus confirming consistency and enabling us to build a wide-range NMRD profile by combination of the results in the same graph (Fig. 3A). Furthermore, high field measurements of the transversal relaxivity (r_2) were performed (Fig. 3B).

Figure 3. A) Nuclear magnetic relaxation dispersion (NMRD) r_1 profile for the S1-4 samples. Inset: Magnified profile of sample S1. Solid lines correspond to the best fitting to the Roch model of the experimental data at 37°C (310 K). B) r_2 profiles for samples S1-4.

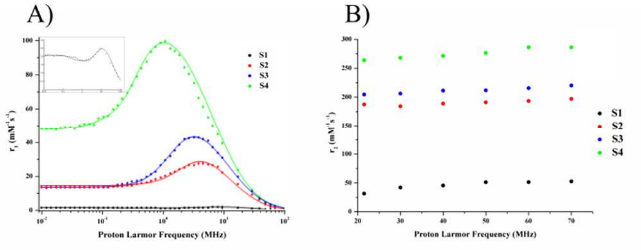

All the measured samples presented a dispersion curve strongly dominated by the effects of superparamagnetic nanoparticles, characterized by a low field plateau followed by a prominent peak in the 1-12 MHz range, referred to as the Curie peak, and by a decrease at high fields (i.e. high Larmor Frequencies). By comparing the profiles, three main differences arise: low field plateau, position of the Curie peak, and maximum relaxivity values. These data were fitted to the equation reported by Roch et al.[26] to describe magnetic resonance relaxation by superparamagnetic agents, which is a widely used model for magnetic nanoparticles and provides a framework to interpret our results. The results of the fit are reported in Fig. 3A, showing a reasonable correspondence with the experimental data obtained for the colloidal suspensions S1-4, which indicates that our nanoparticles are weakly interacting and homogeneously distributed in the solution. The crystal diameter (d), and the saturation magnetization (M_s), which are the main parameters that differentiate our samples, were chosen as fitting parameters; their calculated values are reported in Table 2 and were consistent with the experimental measurements.

Table 2. Main structural, magnetic and relaxometric parameters of samples S1-4. [a] calculated values.

Sample	D core[a] [nm]	M_s[a] [emu g^{-1}]	Curie Peak [MHz]	r_1 max [s^{-1}mM^{-1}]	r_1 @0.01 MHz [s^{-1}mM^{-1}]	r_2 @70 MHz [s^{-1}mM^{-1}]
S1	5.3	35.6	1.22	99.4	47.0	52.7
S2	6.8	52.2	3.62	43.1	14.4	197.0
S3	7.5	55.0	4.37	27.9	13.7	220.3
S4	12.4	60.8	11.34	2.5	2.0	286.1

The relaxation at very low field is governed by the anisotropy energy. For large particles, with high anisotropy energy, the precession of the electron magnetization is forbidden, and the relaxation depends solely on the Néel relaxation time (τ_N) and the Diffusion correlation time (τ_D), which in turns depends on the crystal size (d). Consequently, no dispersion is observed at low fields. On the contrary, when the particles size and, consequently, the anisotropy energy decrease, dispersion at low fields arises. This prediction is consistent with our result, as decreasing the anisotropy energy by decreasing the particle size from sample S4 to S1, the low field dispersion progressively appears (inset of Fig. 3A). The position of the Curie peak occurs at intermediate fields and seems to be strongly dependent on the nanoparticles size, shifting to lower field by increasing the mean crystal size. Such a shift must be ascribed to an increase of the diffusion correlation time (τ_D), which is caused by the observed increase in crystal size, as reported elsewhere. [27]

Finally, our results show a strong increase of the maximum relaxivity value moving from sample S1 to S4. This is interpreted by the theory as the combined result of an increase in M_s and τ_D, as $M_s \propto (R_{max}/C\tau_D)^{1/2}$, where C is a constant.[28]

The good agreement of our PAMAM coated nanoparticles with theory does not only provide information about the relaxometric behaviour, but also allows using the model as a tool to design new contrast agents with optimized relaxometric performance, designed for specific applications, such as low or high field MRI.

As expected for superparamagnetic contrast agents,[29, 30] at high fields the longitudinal relaxivity drastically decreases for all the samples, while the transversal relaxivity dominates their relaxometric behaviour, with values up to 286 s^{-1} mM^{-1} (S4 @70MHz), as it is shown in Fig. 3B. The analysis of the r_2 dispersion shows an almost linear slight increase of relaxivity with the applied magnetic field for all the considered samples, with a significant increase of the relaxivity as a function of the particle size. This is in contrast with previously published works, [24] where any increase of size above 8 nm produces a decrease in r_2, as the consequence of a passage from the so-called "Motional Averaging Regime" (MAR), to the "Static Dephasing Regime" (SDR). This change of regime has been attributed to the strong dipolar field produced by large particles in their surroundings, with r_2 reaching a plateau. In our case, we observe a monotonic increase of r_2 with size, i.e., a MAR regime, where the water diffusion between particles occurs on a much faster time scale than the resonance frequency shift. This seems to indicate that once the particles are dispersed in water, the dipolar interaction observed in the solid state are weak, thus preventing the formation of aggregates. This result is corroborated by the accordance between the observed (table 3) and calculated (table 2) core diameters (table 2), while in case of aggregation the diameters extrapolated from the NMRD dispersion profiles should have been higher.

The simultaneous high transversal and low longitudinal relaxivity displayed by the S1-4 samples accounts for their potentiality as MRI negative contrast agents.

Cell viability

Toxicity is a key parameter which must be evaluated before the use of iron oxide nanoparticles in biomedical applications. In the case of superparamagnetic systems, toxicity can arise both from the inorganic core and the hydrophilic coating, with the former mainly depending on size.

We measured the metabolic activity of bEND5 cells upon exposure of increasing concentrations of S1 and S4, and found that it was not dependent on the core size in the nanomolar range of concentration (Fig. 4).

Figure 4. Metabolic activity after 24 hours of A) S3 and B) S4 as a function of the iron concentration.

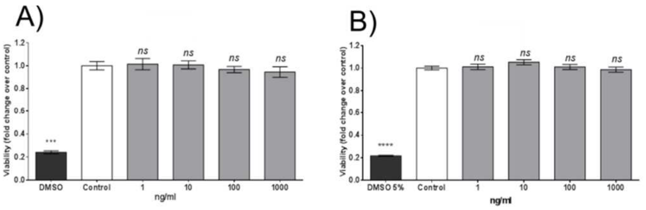

Only S2 demonstrated a slight, albeit statistically significant, decrease in metabolism in presence of $1\mu M$ S2 particles for 24h. On the other hand, S1, S3 and S4 did not show any variation versus untreated controls.

In order to evaluate the effect of the PAMAM coating, we performed a measurement of the metabolic activity of samples A2 and A3, obtained by coating NP 2 and NP 3 with 3-AminoPropylTriEthoxySilane (APTES), a widely used biocompatible coating. Both for PAMAM and APTES coated NPs, no variation versus untreated control was observed up to 1000 ng/mL Fe concentration, demonstrating the biocompatibility of the PAMAM coating (see Fig. S4, Supplementary Material).

After conjugation with a proper fluorophore dye (Atto 633), S4 NPs have also been tested for their cell internalization potential by confocal microscopy and flow cytometry (Fig. 5).

Figure 5. Confocal microscopy images of bEND5 cells A) before and B) 2h after administration of Atto 633-labelled S4 samples; C) Confocal microscopy image evidencing s the co-localization of S4 with lysosomes; D) Flow cytometry measurement of internalization on S4.

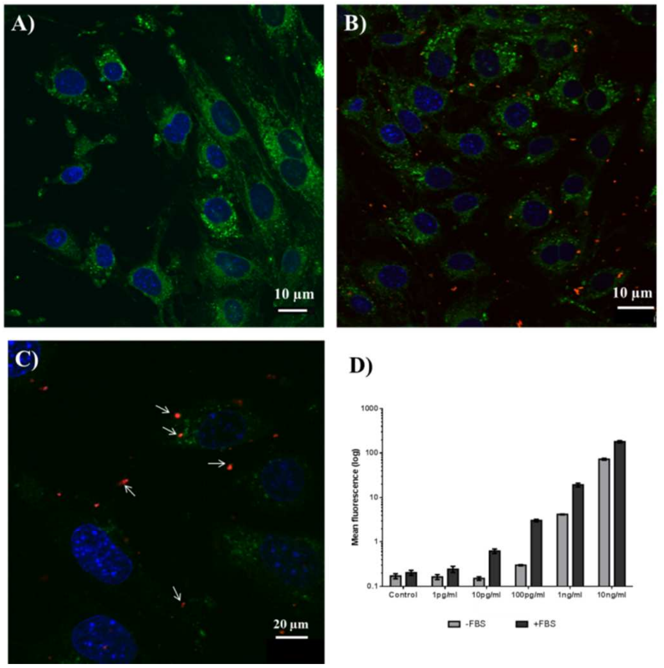

2h after the administration Atto 633-labelled S4 entered the endothelial cell as shown in Fig. 5A and Fig. 5B. Moreover, the analysis of co-localization with lysosomes demonstrated the presence of the nanoparticles within the acidic vesicles (Fig. 5C). This observation suggests that S4 internalization likely happens through the endocytic pathway. Since endocytosis of many nanoparticles is dependent on the type of culture medium,[31] we quantified the internalization by flow cytometry in presence and absence of serum. As shown in Fig. 5D, the presence of 10% serum in the culture medium induce a dramatic increase in S4 internalization at all the nanoparticle concentration tested. This may be likely due to the protein corona enhanced endocytosis.

The internalization of S4 was also explored *via* the Ultrastructural Characterization of NPs treated U2OS cells (Fig. 6).

Figure 6. A) TEM micrograph of U2OS treated 24 h with S4 NPs 10 ng/ml. The NPs aggregate surrounded by endosomal membrane is close to the nuclear envelope. Cytoplasmic organelles do not show any sign of alteration. Inset shows a higher magnification of an aggregate of S4 NPs. B) Polycrystalline electron diffraction pattern collected by illuminating a single NPs aggregate. The pattern can be indexed with a cubic, face-centered, magnetite structure. Indices of the main visible rings are reported C). Aggregate of S4 NPs next to nucleus of U2OS cell treated 24 h with a 100 ng/ml NPs solution. The cellular architecture does not show any sign of alteration. D) Image of U2OS cell treated 24h with 1 µg/mL solution of S4 NPs, taken in a region comparable to A) and C). In the perinuclear space altered organelles, swollen Golgi stacks as well as damaged mitochondria are clearly visible.

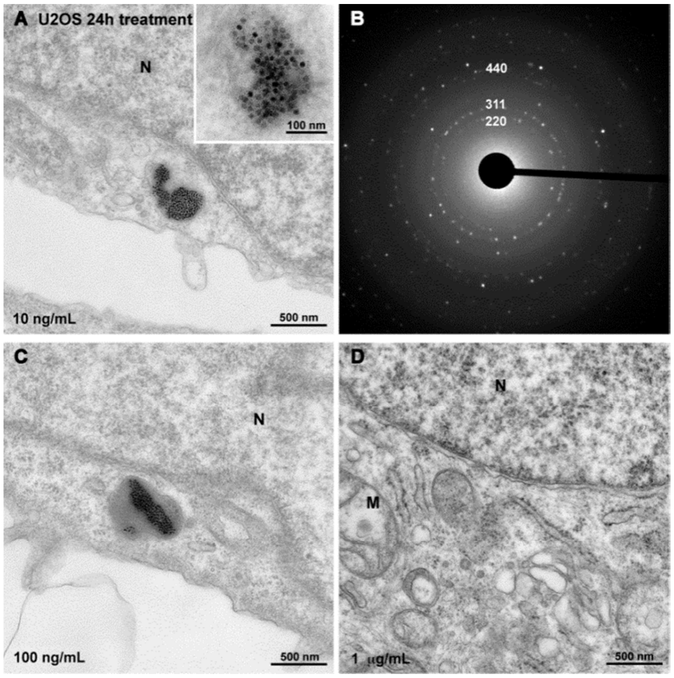

We analysed the ultrastructure of U2OS cells treated with growing concentration of S4 compared with untreated cells. The largest majority (around 90%) of U2OS cells, treated 24h with a suspension of 10 ng/mL S4 in medium, was positive for the presence of NPs showing one to three NPs aggregates per cell. We found nor isolated particles within cells, neither free particles in the cytoplasm. Nanoparticles were located in the endosomal compartment without a preferential localization within the cell (Fig. 6A). No signs of nuclear internalization were observed even if the majority of aggregates were found in the perinuclear space. The treatment seems not to induce alteration in the architecture of cytoskeleton neither in the ultrastructure of cytoplasmic organelles. We observed, just in few cases, mild alteration of mitochondrial inner membrane without variation of the outer one or swelling of the organelle.

At the increased concentration of 100 ng/mL few apoptotic cells were found within the culture (around 5%) but not signs of degeneration were identified in the other cells (Fig. 6C).

However the number of positive cells was significantly reduced compared to 10 ng/mL treated cells.

This effect may be correlated to the large number of cells in M-Phase of the cellular cycle, since no NP aggregates were observed in these cells. Furthermore, in the positive cells 1 to 3 aggregates per cell were detected, with the same distribution observed in the other sample. Finally, we stressed the system by treating U2OS cells 24h with a highly concentrated solution, equal to 1 µg/mL S4 in cellular medium and observed apoptotic effects in this cell line (Fig. 6D). Survived cells showed a reduced number of aggregates and a decreased number of particles per aggregate. We also identified free NPs in the extracellular space that may indicate a release due to cell death, or to a mechanism of exocytosis that would also explain the reduced number of aggregates per cell.

Ultrastructural analysis via TEM confirms that our PAMAM coated nanoparticles are biocompatible at least up to 100 ng/mL, and undergo easy and fast internalization. These results open up to possible in vivo applications of these systems, both as MRI contrast agents and carriers for drugs or targeting units to perform specific targeting and therapy treatments.

Relaxation at clinical fields

Thanks to their high r_2/r_1 ratio at high field, samples S3 and S4 were chosen as the best candidates to provide high performance as MRI contrast agents. Thus, we studied the efficacy of these nanoparticles to enhance the tissue contrast of an area of interest by increasing the relaxation rate of water, with the largest effect being on the T_2 relaxation time.

We detected an increase of R_2 relaxation rates with increasing concentration of the NPs in water solutions (see Supplementary Material, Fig. S5): a linear trend was observed both at the clinical fields of 1.5 and at 3T, allowing estimation of the r_2 relaxivities (mM^{-1} s^{-1}) by the slop of the regression line. The results were in accordance with the previously mentioned FFC measurements, showing a higher transverse relaxation (R_2) with respect to the longitudinal relaxation (R_1), demonstrated by the high r_2 values obtained for all the analysed systems (Table 3). In particular, S4 samples resulted to be more effective than S3 samples, as expected due to difference in size dimensions; indeed, r_2 value resulted to be higher for S4 compared to S3.

		S3			S4		
		r_2(mM^{-1}s^{-1})	r_1(mM^{-1}s^{-1})	r_2/r_1	r_2(mM^{-1}s^{-1})	r_1(mM^{-1}s^{-1})	r_2/r_1
H_2O	1.5 T	212.43	-	-	234.17	-	-
	3 T	219.71	-	-	257.52	-	-
1% Agar gel	1.5 T	196.8	1.76	111.8	244.3	1.53	159.7
	3 T	230.1	0.9	255.7	255.2	0.78	327.2

Both S3 and S4 provided better performance (higher r_2) at higher field.

Table 3. r_1 and r_2 relaxivity values and r_2/r_1 ratios obtained at 1.5 and 3 T for H_2O and 1% agar gel solutions of S3 and S4.

The relaxation properties of S3 and S4 were also evaluated in 1% agar gel, used as tissue-mimicking phantom.[32] The obtained results (Fig. 7) confirm the good relaxation properties of both the analysed NPs, in parallel with previous results obtained for S3 and S4 in water solutions.

Figure 7. R_1 and R_2 relaxation rates obtained at clinical field of 1.5 and 3T for S3 and S4 are reported as a function of NPs concentration in 1% agar solutions.

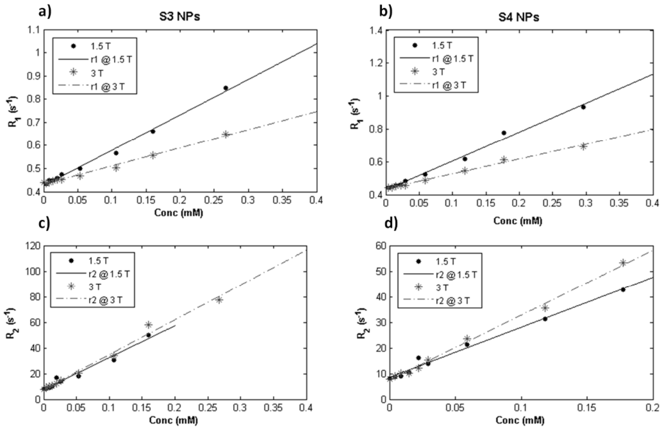

In agreement with relaxivities trends observed in water, we detected a linear dependence of both R_1 and R_2 relaxation rates on the NPs concentration, a higher r_2 with respect to the r_1 for all the analysed systems, and a better performance of S4 (i.e. higher r_2 and slightly lower r_1 values) compared to S3 sample (Table 3).

The ratio r_2/r_1 was selected as an index of MRI contrast enhancement for the S3-4 samples: as reported in Table 3. For both samples, the ratio resulted to be higher at 3 T compared to 1.5 T, and significantly higher with respect to other typical values previously reported for iron oxide NPs,[33] which proves the good potential of S3-4 as negative contrast agents for *in vivo* MRI.

We also evaluated T_2-relaxivity at lower clinical fields, using 0.32 T and 0.5 T open magnets (Paramed Medical System, Genova, Italy) and a dedicated multi-array head coil: r_2 was measured at low field in the same conditions and media. In this case S3 showed better T_2 contrast enhancement (r_2 = 145.7 and 136.1 mM^{-1} s^{-1} at 0.3 and 0.5 T respectively) than S4 (r_2 = 141.7 and 108 mM^{-1} s^{-1} at 0.3 and 0.5 T respectively).

In vivo MRI

In order to evaluate the intended use as multifunctional contrast agents we tested PAMAM coated NPs *in vivo*: we selected S4 NPs because of better contrast enhancement properties as provided by the larger crystalline core (14.1 nm). We evaluated the kinetics of distribution *in vivo* of S4 NPs which have been rapidly extracted from the ReticuloEndothelial System (RES), including the liver and spleen. Fig. 8 shows T_2-weighted MR coronal image of a rat after administration of the S4 NPs, injected at 1 mg kg^{-1} Fe eq. It is worth to note that a rapid and persistent reduction in the MR signals was detected in the rat liver 8-15 min after injection of the S4 NPs.

Figure 8. The transverse relaxation rate R_2 relative to a representative ROI prescribed on the right hepatic lobe is reported over time after injection of S4 bolus sample in the tail vein. A representative coronal T_2-weighted image is also displayed.

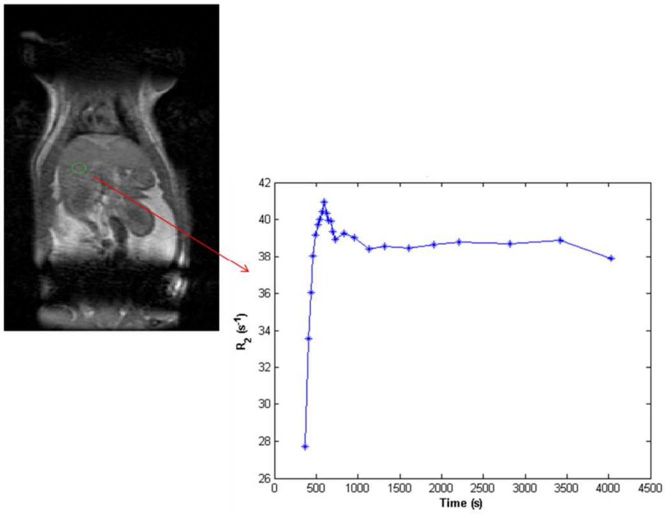

The rapid increase of the transverse relaxation rate (R_2) detected over time for a Region Of Interest (ROI) selected in the right hepatic lobe is also displayed in Fig. 8. The R_2 enhancement affected the overall liver, whereas no significant variation of R_2 over time was detected in organs other than RES, such as kidneys or heart, up to 1 hour after the injection. The signal decrease observed in the rat liver is in good agreement with previous findings with Iron Oxide NPs clinically used and characterized by a hydrodynamic size in the range of 80–150 nm (S4 d_{hyd}=96.1 nm). In fact, these systems are rapidly recognized in the RES of the liver and spleen, resulting in a short plasma half-life.[34] The physiological parameters of the animal were recorded during the study, without any alteration induced by the NPs injection. According these results, the PAMAM coated NPs showed suitable r_2 relaxivity, arising from the particle core, the hydrodynamic size and the coating thickness. These NPs demonstrated to produce a strong reduction in the MR signals in rat liver after injection, indicating that they have potential for use as T_2 MRI contrast agents with significant enhanced sensitivity.

Experimental

Samples preparation

In the preparations, iron pentacarbonyl (Fe(CO)5, 99.5%), oleic acid (OA), dioctyl ether, trimethylamine N-oxide, toluene, ethanol, anhydrous dimethylsolfoxide (DMSO), anhydrous N,N-dimethylformamide (DMF), $GdCl_3{\cdot}6H_2O$, Atto 633, PAMAM generation 4 and PAMAM-C_{12} generation 4 (methanol solution) were purchased from Sigma-Aldrich. Samples were prepared according to the reported method: NP-OAs (13 mg, 83 μmol Fe, 30 μmol OA) were added to a solution of 0.25 mL of PAMAM-C_{12} generation 4 (methanol solution, 20 mg, 1 μmol) in 10 mL of water. After 16 hours stirring solvents were removed under vacuum and replaced by addition of water. 30 minutes of sonication facilitated the dispersion of the powder in water solution, which became orange. Recovery with a magnet allowed removing the unreacted dendrimers and other residues of the reaction.

For the synthesis of gadolinium or Atto 633 labelled NPs, PAMAM C_{12} was previously conjugated with N-hydroxysuccinimide (NHS) derivatives of DOTA (and then reacted with an excess of $GdCl_3{\cdot}6H_2O$ in water) and Atto 633. APTES coated samples were synthesized following literature methods.[35]

Structural and Magnetic Characterization

The measurement of iron and gadolinium content in the samples was performed by an Inductively Coupled Plasma-Mass Spectrometry technique (ICP-MS, Agilent Technologies Inc., 7700 series, USA). Dynamic Light Scattering measurements were performed on a Malvern Nano ZS90 Zetasizer instrument at 298 K. Conventional TEM micrographs and electron diffraction patterns were obtained with a Zeiss Libra 120 TEM operating at 120 kV and equipped with in column Omega filter for energy loss electron spectroscopy (EELS). The NP size distribution histogram was determined using enlarged TEM micrographs taken at magnification of 100 K on a statistical sample of ca. 200 NPs. Magnetization data were collected on dry powder with a Quantum Design Ltd. SQUID magnetometer working in the temperature range of 1.8-350 K and the magnetic field range of 0-5 T. Data were corrected for the diamagnetic contribution, separately measured.

Relaxometry

FFC neasurements Water proton relaxation measurements at fixed frequency were obtained on a StelarSpinMaster Spectrometer (Stelar S.n.c., Mede (PV), Italy) operating in the range 20-70MHz. Water proton T_1 data were obtained by means of the Inversion-Recovery technique (16 experiments, 2 scans). Water proton T_2 data were obtained by means of the CPMG sequence with the following parameters: 8 scans, 2048 data points, delay time equal to 5 times T_1, applying a phase cycle on the pulses. Data were fitted with a monoexponential function. ^{1}H-NMRD (Nuclear Magnetic Relaxation Dispersion) profiles were recorded at 37°C on a StelarSpinmaster-FFC field-cycling relaxometer (StelarS.n.c., Mede (PV), Italy) by measuring water proton longitudinal relaxation rates at magnetic field strengths in the range from $2.4{\cdot}10^{-4}$ to 0.47 T (corresponding to 0.01 to 20 MHz proton Larmor frequencies). Phantoms consisting of H_2O and 1% agar gel solutions of NPs at different concentrations (in the range 0.004 – 0.3 mM, [Fe] concentration) were prepared for the evaluation of the relaxation profile. The measurements were conducted using clinical scanners at 1.5 T (Signa Excite, GE Healthcare, USA) and 3.0 T (Signa HDxT, GE Healthcare, USA) , equipped with a clinical head coil for MR signal detection. [36] The longitudinal (T_1) relaxation time of the solutions was measured using a T_1-weighted MRI sequence based on a standard Inversion Recovery (IR) with the following parameters: TR = 9000, TE = 7.6 ms, TI = 100 – 2100 ms in steps of 200 ms, FOV = 18x18 cm for 3 T and 23x23 cm at 1.5 T, matrix 192x192 pixels, slice thickness = 3 mm.

The transverse (T_2) relaxation time was measured with a T_2-weighted Fast Spin Echo sequence using the following parameters: TR = 4500 ms; TE = 6.7 – 87.2 ms, 16 scans, FOV = 16x16 cm at 3 T and 23x23 cm at 1.5 T, matrix 192x192 pixels, slice thickness = 3 mm. Relaxivities at 0.32 T and 0.5 T were obtained with an open magnet (Paramed Medical System), using a dedicated head multi-array coil.

r_1 and r_2 were assessed from the slope of the linear fit of R_2 versus concentration.

Cell viability

Chemicals: All cell culture media and supplements, fetal bovine serum (FBS), phosphate-buffered saline (PBS) pH 7.4, 0,25% Trypsin/EDTA, and LysoTracker-red D99 were purchased from Life Technologies (Carlsbad, CA, USA). WST-8 cell counting kit, DMSO, 3,3′ -Dihexyloxacarbocyanine iodide (DiOC6) and Hoechst 33258 nuclei staining solution were purchased from Sigma-Aldrich (St Louis, MO, USA).

The metabolic activity of bEND5 cell line was determined 24 h following exposure to NP (0.001–1 • g/ml), using a standard WST-8 assay in 96 multi-well microplates. Cells were seeded at a density of 5000 cells/well and cultured for 24 h in a humidified atmosphere at 37°C and 5% CO_2, before being treated. Overall, 5% DMSO was used as positive control and culture medium as negative. A total of 10 • μL of Cell Counting Reagent WST-8 were added to each well. Following 3 h incubation, the orange WST-8 formazan product was measured by using a Synergy-HT (BioTEK) microplates reader at a wavelength of 460 nm. To express the cytotoxicity, the average absorbance of the wells containing cell culture medium without cells was subtracted from the average absorbance of the solvent control, 5% DMSO or NP-treated cells. The percentage of cell viability was calculated using the following equation:

$$\frac{(Absorbance_{treated} - Absorbance_{culture\ medium})}{(Absorbance_{control} - Absorbance_{culture\ medium})} \times 100$$

Data are expressed as mean ± SE of six replicates from at least three independent experiments. Statistical significance versus controls was calculated using one-way ANOVA with Dunnett's post hoc test (p value < 0.05).

Flow Cytometry: 24 h after being plated in a 12 well-multiwell plate, bEND5 cells were incubated with NP-1-Atto633 at final concentrations ranging from 1 pg/ml to 10 ng/ml, both with or without Fetal Bovine Serum in complete cell culture medium. After 2 h in humidified atmosphere at 37°C and 5% CO_2, cells were detached with 0,25% Trypsin/EDTA and analysed by flow cytometry using a MACSQuant analyzer (Miltenyi Biotec, Bergisch Gladbach, Germany). 20,000 events per point were analyzed in triplicate.

Confocal microscopy: Uptake of NP-1 conjugated with Atto-633 in cells was tracked by Olympus FV100 confocal microscope. To image cell morphology, bEND3 cells were grown on WillCo-dish for 24 hours. Cells were then treated for 2 hours with 1ng/ml of NPs, washed with PBS pH 7.4, fixed in buffered 4% paraformaldehyde for 15 min and incubated with 50 nM DiOC6 for 30 minutes. Hoechst staining solution was subsequently added for 15 min and each sample was mounted with Vectashield (Vector Laboratories, Burlingame, CA, USA). Lysosome-PAMAM co-localisation was obtained with 50 nM LysoTracker-red D99 3 h after NP-1 exposure (1 ng/ml). Then cell was washed with PBS pH 7.4 and fixed in buffered 4% paraformaldehyde. Hoechst staining solution was subsequently added for 15 min on fixed cells, and each sample, mounted with Vectashield, was visualized within 1 hour.

TEM microscopy: We tested the effect of S4 NPs on U2OS cells (human osteosarcoma cell line) and treated them 24 hours with different concentration of nanoparticles solution. After 24h cells were washed and fixed, then treated with a conventional embedding protocol (as previously shown in Ciofani et al., 2013). Briefly U2OS cells were fixed as monolayer (with a solution of 2% glutaraldehyde in cacodylate buffer) then scraped and centrifuged to obtain a stable pellet. Pellets were deeper fixed in the same fixative solution overnight. Subsequently cells were washed in cacodylate buffer, postfixed with osmium tetroxide 2% in the same buffer, then dehydrated with ethanol growing series and embedded in epoxy resin. After resin polymerization (48 hours, 60°C) samples were cut in thin sections (80-90 nm). Sections were collected over 300 mesh copper grids and were analyzed using a Zeiss Libra 120 Plus transmission electron microscope operating at 120 kV and equipped with an in-column omega filter and 16-bit CCD camera 2k x 2k bottom mounted.

In vivo MRI

MRI *in vivo* studies were performed at 3 T using a clinical scanner (Signa HDxT, GE Healthcare, USA) equipped with a dedicated birdcage coil (Rapid Biomedical, Rimpar, Germany). Nanoparticles were diluted in saline solution to obtain a final injectable concentration of approximately 0.5 mg/mL; afterwards 600 μL of NPs in solution were manually injected in bolus in Wistar rats (300 g body weight), from the rat tail vein. Rats were anesthetized using Zoletil® + xylazine (50 and 3 mg/kg respectively). Fast Spin Echo sequence for T_2 mapping was applied for the acquisition with the following parameters: TR = 1000 ms; Echo times = 8; FOV = 17x17 cm, matrix = 224x224 pixels, total acquisition time = 24 sec. Images in axial plane were acquired in sequence for the first 5 minutes after injection; subsequently, the measurement was repeated at increasing time intervals up to 60 minutes from the injection. A ROI was selected on the anatomical district of interest on the image and the corresponding T_2 was measured for each acquisition; the transverse relaxation rate R_2 was then estimated as the inverse of T_2. All the experimental protocols conformed to the "Guiding Principles for Research Involving Animals and Human Beings" approved by the Council of the American Physiological Society and were authorized by the local Ethical Committee after approval from Ministry of Health.

Conclusions

In this paper, we provided a general approach to the design of a new class of iron oxide nanoparticles based on the PAMAM dendrimer. A large number of parameters needed for a complete evaluation of their potential use for biomedical applications, e.g. structural, magnetic and relaxometric behavior, biocompatibility and cell internalization, *in vivo* MRI, were collected and discussed in a unique and consistent framework, including an interpretation of the data along a theoretical model.

In summary, iron oxide NPs with a size ranging from 2.6 to 14.1 nm were prepared and coated with lipid modified PAMAM dendrimers to obtain stable water suspensions. Thanks to the mild reaction conditions, the high crystallinity and magnetic moment of the particles were preserved. The acquisition of longitudinal relaxivity NMRD profiles allowed to correlate the relaxometric properties with the magnetic and structural measurements, providing a tool to design iron oxide nanoparticles with the desired relaxometric efficacy by tuning their size and saturation magnetization. Both the r_2 profile and the TEM micrographs suggest the absence of aggregates in water solution. In vitro cell viability tests showed poor toxicity of this material up to 1 μg/mL, with results similar to those obtained with widely used coatings, all over the considered size range. Moreover, confocal and TEM microscopy prooved a high internalization of PAMAM coated nanoparticles, which prefigures the possibility of using this material to build a theranostic targeted device through conjugation with drugs, fluorophores or proteins, as previously reported.[10] Due to their high r_2/r_1 ratio, especially exhibited by the 14.1 nm sized nanoparticles, we performed *in vivo* tests which demonstrated the possibility to detect the nanoparticles *via* MRI. Further work must be carried out in order to prolong the life span of the nanoparticles in the blood stream, which may be performed by conjugation with stealth peptides or by decreasing the size of the nanoparticles, limiting the rethiculoendothelial system (RES) recognition. However, PAMAM coated nanoparticles constitute a promising, versatile material for the development of multifunctional biomedical devices detectable *via* MRI, which can be easily multi-functionalized with any biological moiety (including thermally unstable or water insoluble molecules) for specific biomedical applications and whose relaxometric properties can be modulated by changing the synthesis conditions.

Acknowledgements

The acknowledgements come at the end of an article after the conclusions and before the notes and references.

Notes and references

[a] Istituto Italiano di Tecnologia, Center for Nanotechnology Innovation @NEST, Piazza San Silvestro 12, 56127 Pisa, Italy.
[b] Istituto italiano di Tecnologia, Center for Biomolecular Nanotechnologies @UniLe, Via Barsanti 1, 73010 Arnesano (Lecce), Italy.
[c] University of Pisa, Department of Biology, Unit of Cell and Developmental Biology, Via Ghini, 13, 56126 Pisa, Italy.
[d] Istituto Italiano di Tecnologia, Center for Neuroscience and Cognitive Systems @ UniTn, Corso Bettini 31, 38068 Rovereto, Italy.
[e] Fondazione CNR/Regione Toscana G.Monasterio, Via Moruzzi, 1, 56124 Pisa, Italy.
[f] INSTM and Department of Chemistry "Ugo Schiff", University of Florence, via della Lastruccia 3-13, 50019 Sesto F. no, Firenze, Italy.
[g] CNR Institute of Clinical Physiology, Via Moruzzi, 1, 56124 Pisa, Italy.
[h] CNR-ISTM and INSTM, via Golgi 19, 20133 Milano, Italy.

1. L. H. Reddy, J. L. Arias, J. Nicolas and P. Couvreur, *Chemical reviews*, 2012, **112**, 5818-5878.
2. R. Qiao, C. Yang and M. Gao, *Journal of Materials Chemistry*, 2009, **19**, 6274-6293.
3. E. Terreno, D. D. Castelli, A. Viale and S. Aime, *Chemical reviews*, 2010, **110**, 3019-3042.
4. E. C. Cho, C. Glaus, J. Chen, M. J. Welch and Y. Xia, *Trends in molecular medicine*, 2010, **16**, 561-573.
5. L. Yang, H. Kuang, W. Zhang, Z. P. Aguilar, Y. Xiong, W. Lai, H. Xu and H. Wei, *Nanoscale*, 2014.
6. S. Sun and H. Zeng, *Journal of the American Chemical Society*, 2002, **124**, 8204-8205.
7. J. Rockenberger, E. C. Scher and A. P. Alivisatos, *Journal of the American Chemical Society*, 1999, **121**, 11595-11596.
8. H. Qu, H. Ma, A. Riviere, W. Zhou and C. J. O'Connor, *Journal of Materials Chemistry*, 2012, **22**, 3311-3313.
9. T. Hyeon, S. S. Lee, J. Park, Y. Chung and H. B. Na, *Journal of the American Chemical Society*, 2001, **123**, 12798-12801.
10. A. Boni, L. Albertazzi, C. Innocenti, M. Gemmi and A. Bifone, *Langmuir : the ACS journal of surfaces and colloids*, 2013, **29**, 10973-10979.
11. L. Albertazzi, M. Serresi, A. Albanese and F. Beltram, *Molecular Pharmaceutics*, 2010, **7**, 680-688.
12. R. K. Tekade, P. V. Kumar and N. K. Jain, *Chemical reviews*, 2008, **109**, 49-87.
13. C. C. Lee, J. A. MacKay, J. M. Frechet and F. C. Szoka, *Nat Biotechnol*, 2005, **23**, 1517-1526.
14. I. J. Majoros, A. Myc, T. Thomas, C. B. Mehta and J. R. Baker, *Biomacromolecules*, 2006, **7**, 572-579.
15. C. C. Lee, E. R. Gillies, M. E. Fox, S. J. Guillaudeu, J. M. J. Fréchet, E. E. Dy and F. C. Szoka, *Proceedings of the National Academy of Sciences*, 2006, **103**, 16649-16654.
16. J. Zhou, J. Wu, N. Hafdi, J.-P. Behr, P. Erbacher and L. Peng, *Chemical Communications*, 2006, **0**, 2362-2364.
17. M. A. Mintzer and E. E. Simanek, *Chemical reviews*, 2008, **109**, 259-302.
18. A.-M. Caminade, C.-O. Turrin and J.-P. Majoral, *Chemistry – A European Journal*, 2008, **14**, 7422-7432.
19. H. Xu, C. A. S. Regino, Y. Koyama, Y. Hama, A. J. Gunn, M. Bernardo, H. Kobayashi, P. L. Choyke and M. W. Brechbiel, *Bioconjugate Chemistry*, 2007, **18**, 1474-1482.

20. H. Kobayashi, Y. Koyama, T. Barrett, Y. Hama, C. A. S. Regino, I. S. Shin, B.-S. Jang, N. Le, C. H. Paik, P. L. Choyke and Y. Urano, *ACS Nano*, 2007, **1**, 258-264.
21. A. H. Morrish, *The Physical Principles of Magnetism*, John Wiley and Sons, New York, 1965.
22. A.-H. Lu, E. L. Salabas and F. Schüth, *Angewandte Chemie International Edition*, 2007, **46**, 1222-1244.
23. A. Boni, M. Marinone, C. Innocenti, C. Sangregorio, M. Corti, A. Lascialfari, M. Mariani, F. Orsini, G. Poletti and M. F. Casula, *Journal of Physics D: Applied Physics*, 2008, **41**, 134021.
24. M. F. Casula, P. Floris, C. Innocenti, A. Lascialfari, M. Marinone, M. Corti, R. A. Sperling, W. J. Parak and C. Sangregorio, *Chemistry of Materials*, 2010, **22**, 1739-1748.
25. A. Ouakssim, S. Fastrez, A. Roch, S. Laurent, Y. Gossuin, C. Piérart, L. Vander Elst and R. N. Muller, *Journal of Magnetism and Magnetic Materials*, 2004, **272–276, Supplement**, E1711-E1713.
26. A. Roch, R. N. Muller and P. Gillis, *Journal of Chemical Physics*, 1999, **110**, 5403-5411.
27. A. Boni, D. Ceratti, A. Antonelli, C. Sfara, M. Magnani, E. Manuali, S. Salamida, A. Gozzi and A. Bifone, *Contrast Media & Molecular Imaging*, 2014, **9**, 229-236.
28. S. Laurent, D. Forge, M. Port, A. Roch, C. Robic, L. Vander Elst and R. N. Muller, *Chemical reviews*, 2008, **108**, 2064-2110.
29. T. Heidt and M. Nahrendorf, *NMR in Biomedicine*, 2013, **26**, 756-765.
30. H. B. Na, I. C. Song and T. Hyeon, *Advanced Materials*, 2009, **21**, 2133-2148.
31. I. M. Adjei, B. Sharma and V. Labhasetwar, *Advances in experimental medicine and biology*, 2014, **811**, 73-91.
32. A. Hellerbach, V. Schuster, A. Jansen and J. Sommer, *PloS one*, 2013, **8**, e70343.
33. A. Ruiz, G. Salas, M. Calero, Y. Hernández, A. Villanueva, F. Herranz, S. Veintemillas-Verdaguer, E. Martínez, D. F. Barber and M. P. Morales, *Acta Biomaterialia*, 2013, **9**, 6421-6430.
34. A. Tanimoto, K. Oshio, M. Suematsu, D. Pouliquen and D. D. Stark, *Journal of Magnetic Resonance Imaging*, 2001, **14**, 72-77.
35. N. R. Jana, C. Earhart and J. Y. Ying, *Chemistry of Materials*, 2007, **19**, 5074-5082.
36. L. Menichetti, L. Manzoni, L. Paduano, A. Flori, C. Kusmic, D. De Marchi, S. Casciaro, F. Conversano, M. Lombardi, V. Positano and D. Arosio, *Sensors Journal, IEEE*, 2013, **13**, 2341-2347.